International Journal of Nanomedicine

Dovepress
open access to scientific and medical research

Open Access Full Text Article

ORIGINAL RESEARCH

A Multifunctional, Highly Biocompatible, and Double-Triggering Caramelized Nanotheranostic System Loaded with Fe_3O_4 and DOX for Combined Chemo-Photothermal Therapy and Real-Time Magnetic Resonance Imaging Monitoring of Triple Negative Breast Cancer

Fangqing Wang[1,*], Nianlu Li[2,*], Wenbo Wang[1], Long Ma[3], Yaru Sun[4], Hong Wang[1], Jinhua Zhan[5], Dexin Yu[1]

[1]Department of Radiology, Qilu Hospital, Shandong University, Affiliated Hospital of Shandong University, Jinan, 250012, People's Republic of China; [2]Physical and Chemical Laboratory, Shandong Academy of Occupational Health and Occupational Medicine, Affiliated Hospital of Shandong First Medical University & Shandong Academy of Medical Sciences, Jinan, 250002, People's Republic of China; [3]The Testing Center of Shandong Bureau of China Metallurgical Geology Bureau, Shandong Normal University, Jinan, 250014, People's Republic of China; [4]Department of Nuclear Medicine, The Second Hospital of Shandong University, Affiliated Hospital of Shandong University, Jinan, 250033, People's Republic of China; [5]School of Chemistry and Chemical Engineering, Shandong University, Jinan, 250100, People's Republic of China

*These authors contributed equally to this work

Correspondence: Jinhua Zhan, School of Chemistry and Chemical Engineering, Shandong University, Jinan, 250100, People's Republic of China, Email jhzhan@sdu.edu.cn; Dexin Yu, Department of Radiology, Qilu Hospital, Shandong University, Affiliated Hospital of Shandong University, Jinan, 250012, People's Republic of China, Tel +86-18560081629, Fax +86-531-86927544, Email yudexin0330@sina.com

Purpose: Owing to lack of specific molecular targets, the current clinical therapeutic strategy for triple negative breast cancer (TNBC) is still limited. In recent years, some nanosystems for malignancy treatment have received considerable attention. In this study, we prepared caramelized nanospheres (CNSs) loaded with doxorubicin (DOX) and Fe_3O_4 to achieve the synergistic effect of combined therapy and real-time magnetic resonance imaging (MRI) monitoring, so as to improve the diagnosis and therapeutic effect of TNBC.

Methods: CNSs with biocompatibility and unique optical properties were prepared by hydrothermal method, DOX and Fe_3O_4 were loaded on it to obtain Fe_3O_4/DOX@CNSs nanosystem. Characteristics including morphology, hydrodynamic size, zeta potentials and magnetic properties of Fe_3O_4/DOX@CNSs were evaluated. The DOX release was evaluated by different pH/near-infrared (NIR) light energy. Biosafety, pharmacokinetics, MRI and therapeutic treatment of Fe_3O_4@CNSs, DOX and Fe_3O_4/DOX@CNSs were examined in vitro or in vivo.

Results: Fe_3O_4/DOX@CNSs has an average particle size of 160 nm and a zeta potential of 27.5mV, it demonstrated that Fe_3O_4 /DOX@CNSs is a stable and homogeneous dispersed system. The hemolysis experiment of Fe_3O_4/DOX@CNSs proved that it can be used in vivo. Fe_3O_4/DOX@CNSs displayed high photothermal conversion efficiency, extensive pH/heat-induced DOX release. 70.3% DOX release is observed under the 808 nm laser in the pH = 5 PBS solution, obviously higher than pH = 5 (50.9%) and pH = 7.4 (less than 10%). Pharmacokinetic experiments indicated the t1/2β, and AUC_{0-t} of Fe_3O_4/DOX@CNSs were 1.96 and 1.31 -fold higher than those of DOX solution, respectively. Additionally, Fe_3O_4/DOX@CNSs with NIR had the greatest tumor suppression in vitro and in vivo. Moreover, this nanosystem demonstrated distinct contrast enhancement on T2 MRI to achieve real-time imaging monitoring during treatment.

Conclusion: Fe_3O_4/DOX@CNSs is a highly biocompatible, double-triggering and improved DOX bioavailability nanosystem that combines chemo-PTT and real-time MRI monitoring to achieve integration of diagnosis and treatment of TNBC.

Keywords: caramelized nanotheranostic system, combining chemo-photothermal therapy, magnetic resonance imaging monitoring, double-triggering, triple negative breast cancer

Received: 20 October 2022
Accepted: 14 February 2023
Published: 19 February 2023

Introduction

Breast cancer is one of the commonly diagnosed cancer in the world and the disease is the leading cause of cancer mortality in women worldwide.[1] The triple negative breast cancer (TNBC) subtype is defined by the lack of expression of estrogen receptor, progesterone receptor and human epidermal growth factor receptor 2.[2] Clinical management of TNBC is a great challenge because of its strong invasiveness, large heterogeneity, and high malignancy.[3,4] Except for surgical resection for early-stage tumors,[5,6] other methods including radiotherapy, chemotherapy, endocrine and targeted therapy are usually limited by poor targeting, multidrug resistance (MDR), and side effects that cause serious damage to non-cancerous tissues.[7–10] At present, combination therapy is the main route to improve the curative effect of TNBC; however, the overall survival rate is still not high, and the side effects are cumulative.[11] In the diagnosis and assessment of the treatment efficacy, non-invasive imaging methods including ultrasound, mammography, computed tomography (CT) and magnetic resonance imaging (MRI).[12] Among these, MRI is readily available, non-invasive, does not rely on the use of ionizing radiation, has high spatial resolution, soft tissue and spatial resolution.[13] However, the common MRI contrast agent currently used in clinical practice is non-specific with neurotoxicity and nephrotoxicity.[14] Therefore, a targeted and safe MRI contrast agent is emerging as a major clinical requirement for imaging diagnosis and monitoring.

With the development of nanomedicine in the last few decades, the multifunctional and multimodal theragnostic nano-platform has shown immense potential in combining treatment and diagnosis with synergetic reinforcing effects for malignant tumors in recent years and can aid in overcoming the challenges with the diagnosis and treatment of TNBC. However, some problems remain, such as the nanocarrier toxicity, complicated combination modalities, and interference from different components, which may limit its clinical translation and application.[15–17]

In recent years, photothermal therapy (PTT) has emerged as a novel cancer treatment that uses photothermal therapy agents (PTAs) to absorb near-infrared (NIR) light energy and convert this into heat energy, causing local overheating to thermally ablate target cells while causing minimal damage to the surrounding normal cells and tissues.[18,19] Moreover, PTT-derived multimodal combination treatments have received extensive attention and exhibited cooperatively enhanced anticancer effects. Some new nanomaterials such as those based on gold, carbon, and manganese have excellent NIR absorption efficiency, and could be considered as candidate materials for PTAs.[20–22] However, the unknown toxicity and biocompatibility hinder their use in long-term clinical studies.[23] Our previous studies have shown that food-grade caramelized nanospheres (CNSs) are safe carriers in biological applications with high biocompatibility and low toxicity,[24] and their robust π-π conjugated structure could act as excellent NIR light absorbing agents for PTT.[25] The rich functional groups (hydroxyl and carboxyl groups) on their surface can interact easily with PTAs and antitumor drugs.[24,26] In addition, superparamagnetic Fe_3O_4 nanoparticles (NPs) with less expensive to produce, good biocompatibility and low toxicity, approved by the USA Food and Drug Administration (FDA),[27–33] also offer a high photothermal conversion efficiency and T2-relaxation effects for MRI, demonstrating suitable combining theragnostic effects for PTT and real-time MRI monitoring of the treatment.[27–29] Moreover, CNSs, in combination with PTT and conventional chemotherapy using doxorubicin hydrochloride (DOX), may achieve pH/NIR sensitive drug release, thereby significantly enhancing local drug enrichment in the tumor and reducing adverse effects at lower drug doses.[17]

In the present study, we successfully synthesized a multifunctional nanosystem, Fe_3O_4/DOX@CNSs, to realize combination chemo-PTT treatment and real-time MRI monitoring for improved TNBC treatment. In this system, the Fe_3O_4/DOX@CNSs Fe3O4/DOX@CNSs has longer circulation and strong ability to transform incident 808 nm NIR light into heat energy for photothermal drug release; it is also an appealing candidate for future nanomedicine translation due to their accurate MR imaging properties and effective combination with PTT.

Experimental

Materials and Reagents

All reagents were commercially available. Ferric trichloride hexahydrate ($FeCl_3 \cdot 6H_2O$), ammonium hydroxide ($NH_3 \cdot H_2O$), and D-(+)-glucose were purchased from Sinopharm Chemical Reagent Co., Ltd (China). Ferrous chloride tetrahydrate ($FeCl_2 \cdot 4H_2O$) was obtained from Aladdin Chemical Reagent Co., Ltd (China). Deionized water (18.25 MΩ·cm) was used during the experiment. Phosphate buffered saline (PBS) (pH = 6.5) and DOX were purchased from Beijing solarbio Science and Technology Co., Ltd (China). 1-(3-Dimethylaminopropyl)-3-ethylcar bodiimide hydrochloride (EDC) and

N-Hydroxysuccinimide (NHS) were obtained from Beijing Fine Chemical Regent Co., Ltd. (China). The 4T1 (Mouse breast cancer) cell line, MCF-10A (Mammary epithelial) cell line and THP-1 (Human mononuclear) cell lines were purchased from icell Bioscience Inc (Shanghai, China).

Experimental Apparatus

The morphology was characterized by transmission electron microscopy (JEM-2100, JEOL, Japan) and scanning electron microscopy (JEM-6700F, JEOL, Japan) with an energy dispersive spectroscope (EDS). The zeta potentials and size distribution of nanomaterials dispersed in water were determined on a Malvern Zetasizer Nano ZS (Malvern Instruments Ltd., Worcestershire, U.K.). The content of Fe was measured by inductively coupled plasma-atomic mass spectrometry (ICP-MS, Becton Dickinson, USA). Absorption spectra were captured by an ultraviolet (UV) spectrophotometer (TU-1901, Puxi General Instrument Co., Ltd. Beijing, China). The X-ray diffraction (XRD) was investigated on an advanced X-ray diffractometer (Bruker D8, Bruker, Germany) with graphite monochromatized Cu Kα radiation (λ=1.5418 Å). The magnetic properties were determined using a multifunctional vibrating sample magnetometer (VSM, VersalLab) at room temperature. The UV-visible spectra were measured using a U3900 spectrophotometer (Hitachi, Tokyo, Japan). MRI scanning was conducted using a 3.0 T MRI instrument (GE Signa HDX 3.0T, USA). The optical density (OD) of the cells was measured using a multifunctional microplate reader (Molecular Devices Co., USA). Temperature measurements were recorded using an IR thermal camera (S6-a, IRS, China). Cell images were captured using a biological microscope (BX-53, Olympus, Japan). The concentration of DOX in Fe_3O_4/DOX@CNSs was determined by high performance liquid chromatography (HPLC, Shimadzu Technologies, Kyoto, Japan).

Synthesis of CNSs

CNSs were prepared according to our report.[34] Briefly, 4 g D-(+)-glucose was dissolved in 35 mL water and the solution was heated and kept at 180°C for 6 h. Finally, the brown products were centrifuged (12,000 rpm, 10 min) and the substrate was washed with ethanol and water. The obtained product was dried in vacuum for further use.

Synthesis of Fe_3O_4

Fe_3O_4 NPs were prepared as follows:[34] 0.28 mmol of $FeCl_3{\cdot}6H_2O$ and 0.20 mmol $FeCl_2{\cdot}4H_2O$ were dissolved in 40 mL of deionized water with a stream of N_2 to remove O_2. The mixture was heated and kept at 80°C for 1 h, following which 3 mL of $NH_3{\cdot}H_2O$ was added dropwise. After cooling to room temperature, the product was separated using a magnet and washed with water until the solution pH was neutral. The final sample was dried for further use.

Synthesis of Fe_3O_4@CNSs

First, a 100 mL CNS suspension (0.4 mg/mL) was mixed with a 50 mL Fe_3O_4 solution (0.2 mg/mL) using ultrasonication for 1 h. Subsequently, 1 mL glutaraldehyde was added, and the solution was stirred for another 6 h at room temperature. Finally, the solution was allowed to separate for 10 min and the upper layer was obtained by magnetic separation. The obtained Fe_3O_4@CNSs were washed with ethanol and water and dried for further use. The loading of Fe_3O_4 was calculated using equation:

$$\text{loading capacity}(\text{mg/g}) = \frac{m0 \times 1.38}{m1}$$

where m0 is the Fe detected by ICP-AES and m1 is the amount of CNSs injected.

Synthesis of Fe_3O_4/DOX@CNSs

10 mg Fe_3O_4@CNSs (Fe content of 660 mg/g) was dispersed in 50 mL of PBS under ultrasonication, and 10 mg DOX was added under vigorous stirring for 12 h. The product was separated by a magnet and washed with water. Finally, the dried Fe_3O_4/DOX@CNSs were stored at 4°C in the dark for further use. The loading of DOX was calculated using equation:

$$\text{loading capacity}(\text{mg/g}) = \frac{m2 - m3}{m4}$$

where m2 is the total drug injected, m3 is drug in supernatants and m4 is Fe_3O_4@CNSs injected.

2.7. pH/NIR Triggered Drug Release

The Fe_3O_4/DOX@CNSs were dispersed in 2 mL of pH = 7.4 or 5.0 PBS, and then shaken gently for pH-responsive drug release assay. The solution was centrifuged for a predetermined time, the original PBS was replaced with 2 mL of fresh PBS, and the UV-vis absorption of PBS was measured at a wavelength of 480 nm. Likewise, an 808 nm laser detector was installed 3 cm from the tube core in which the PBS solution was Fe_3O_4/DOX@CNSs (pH = 7.4 or 5.0). Specimens were irradiated with 808 nm NIR light for 5 min and then centrifuged at 7000 rpm for 4 min. Quantification of released free DOX by UV-vis spectroscopy at 480 nm wavelength.[35]

MRI of Fe_3O_4/DOX@CNSs in Solution

The Fe_3O_4/DOX@CNSs were mixed in 1 mL normal saline (NS) to obtain different Mn2þ concentrations (0.12, 0.24, 0.59, 1.19, 1.78, and 2.38 mM), and pure NS was used as a control. All groups underwent 3.0 T MRI scanning. T2 images and T2 relaxation times with the following parameters were acquired using fast spin echo (FSE) sequences: repetition time (TR): 10, 20, 40, 60, 80, and 100 ms; echo time (TE): 10 ms. Different Fe^{3+} relaxation times with different concentrations (0, 0.1, 0.2, 0.3, 0.4, and 0.5 mM) were obtained by linear fitting. The goodness-of-fit was calculated.

Cytotoxicity of Fe_3O_4@CNSs and the Combination Chemo-PTT Therapy of Fe_3O_4 /DOX@CNS in vitro

The cytotoxicity of Fe_3O_4@CNSs was assessed using the Cell Counting Kit 8 (CCK-8) method. MCF-10A and 4T1 cells were seeded in 96-well plates (8000 cells per well) and treated with Fe_3O_4@CNSs in various concentrations (0, 50, 100, and 200 μg/mL) for different durations (12, 24, 36, and 48 h); five compound wells were set up in each group. Subsequently, the wells were washed thrice with PBS, 100 μL CCK-8 was added, and the wells were incubated at 37°C for 40 min. The OD value was measured by a multifunctional microplate reader at 490 nm. The viability of the blank control group was considered as 100%.

4T1 cells were seeded in 96-well plates (8000 cells per well) and treated with the culture medium containing the desired amount of free DOX (1.56, 3.12, 6.25, 12.5, and 25 μg/mL) and Fe_3O_4@CNS (0, 50, 100, and 200 μg/mL). For the photothermal heating experiments, after 4 h of incubation, excess unbound Fe_3O_4@CNSs or Fe_3O_4/DOX@CNSs was removed by rinsing three times with PBS. A fresh culture medium was then added into the wells. The cells were exposed to NIR light (808 nm laser, 1.5 W/cm^2) for 5 min to conduct photothermal or chemo-PTT treatments. Finally, the viabilities of the 4T1 cells were measured by a multifunctional microplate reader at 490 nm.

Hemolysis Testing and in vitro Quantitative Cellular Uptake of Fe_3O_4/DOX@CNSs

To test the hemolysis of Fe_3O_4/DOX@CNSs, 10 mL of rabbit blood was collected from the cardiac apex, following which 0.1 mL of potassium oxalate anticoagulant was added, and 10 mL NS was added to obtain diluted anticoagulant rabbit blood. Fe_3O_4/DOX@CNSs were mixed into 1 mL NS to produce different concentrations (10, 50, 100, and 200 mg/mL). NS was used as a negative control and double-distilled water (DDW) was used as a positive control. All tubes were placed in a 37°C water bath. After preheating for 30 min, 0.3 mL of anticoagulant rabbit blood was added to each tube and the solution was placed in a 37°C water bath for another 60 min. The samples were then centrifuged (1200 rpm, 5 min). The supernatant was transferred into a colorimetric dish to measure the OD at 545 nm. The hemolysis rate (HR) was calculated as HR (%) = (OD mean of the sample to be tested - OD mean of negative control)/(OD mean of positive control - OD mean of negative control) × 100%. According to the GB/T 14233.2 standard (Test methods for infusion, transfusion, injection equipment for medical use – Part 2: Biological test methods), if the HR is less than 5%, it indicates that the material has no hemolysis and meets the hemolysis test requirements of medical materials.

To quantify the capacity of 4T1, MCF-10A, and THP-1 cells to intake Fe_3O_4/DOX@CNSs, the three kinds of cells were inoculated into 6-well plates (3 compound wells were set up in each group). The medium was replaced with Fe_3O_4 /DOX@CNSs (80 mg/mL), the control group used PBS, and the cells were incubated for another 4 h. Finally, the cells were washed thrice with PBS, digested with trypsin, centrifuged, counted, and dissolved in aqua regia for digestion for 3 days. The volume was constant at 5 mL, and the Fe content was analyzed by ICP-MS.

Vitro and in vivo Photothermal Performance of Fe_3O_4/DOX@CNSs

Different concentrations of Fe_3O_4/DOX@CNSs (0, 100, 200, 400, and 600 μg/mL) were irradiated by an 808 nm laser (1.5 W/cm^2) for 10 min in a quartz cuvette. During irradiation, the temperature of solutions was recorded using an IR thermal camera. Furthermore, to determine the photothermal stability, 100 mg/mL of Fe_3O_4/DOX@CNSs was irradiated for 5 min (808 nm laser, 1.5 W/cm^2) and naturally cooled. Ten cycles of control on/off irradiation were performed with the laser (808 nm laser, 1.5 W/cm^2).

All animal experiments were performed in compliance with the ethical guidelines established by the Ethics Committee on Scientific Research of Shandong University Qilu Hospital. Animal care was following the Laboratory Animals-Guidelines for ethical review of animal welfare in China (GB/T 35892-2018). Female BALB/c mice aged 6–8 weeks were purchased from Jinan Peng Yue Laboratory Animal Co., Ltd (Jinan, China). NS and Fe_3O_4/DOX@CNSs (4 mg Fe/kg) were injected into the tail vein of 4T1 tumor-bearing mice (4T1 cells were injected into the right hind legs of healthy BALB/c mice for approximately 10 days). The tumors were irradiated by an 808 nm laser (1.5 W/cm^2) for 10 min, 24 h after injection. Thereafter, they were irradiated every 2 days and over a 14-day period. The tumor temperatures in the different groups were measured.

Vivo MRI Monitoring

The in vivo monitoring experiments were performed using a 3.0 T MRI scanner on 4T1 tumor-bearing BABL/c mice after tail vein injection with 0.1 mL Fe_3O_4/DOX@CNSs (4 mg Fe/kg of body weight). The T2 sequence of the FSE sequence was TR: 2800 ms, TE: 72 ms; flip angle: 90°; slice thickness: 2.0 mm; and field of view: 120 mm. The MR images of mice were obtained at preinjection and different time intervals (0, 3, 12, 24, 48, and 72 h) after the injection of Fe_3O_4/DOX@CNSs.

Vivo Blood Circulation and Biodistribution of Fe_3O_4/DOX@CNSs

Biodistribution assays were performed on 4T1 tumor-bearing mice after tail vein injection of Fe_3O_4/DOX@CNSs (4 mg Fe/kg of body weight). Major organs (hearts, livers, spleens, lungs, kidneys, brains, and tumors) were harvested dried and ground at different time intervals (6, 12, and 24 h; 3 mice per interval) and dissolved by aqua regia for ICP-MS measurement to detect. Three 4T1 tumor-bearing mice injected with NS were used as the control. Additionally, blood was then collected 30 μL from the tail of the mice after injection of Fe_3O_4/DOX@CNSs (4 mg Fe/kg of body weight) at different time intervals (5 min, 15 min, 1, 2, 4, 8, 12, 24, and 48 h; 3 mice per interval). The Fe^{3+} levels were measured by ICP-MS after blood samples were digested in aqua regia for 3 days. Finally, the amount of Fe^{3+} in the above organs of interest is expressed in terms of the percentage if injection dose per gram (% ID/g).

In vivo Pharmacokinetics Study

All animal experiments were performed in compliance with the ethical guidelines established by the Ethics Committee on Scientific Research of Shandong University Qilu Hospital. Animal care was following the Laboratory Animals-Guidelines for ethical review of animal welfare in China (GB/T 35892-2018). Healthy SD rats (200 ± 20 g) were purchased from Jinan Peng Yue Laboratory Animal Co., Ltd (Jinan, China). Six male SD rats were randomly divided into two groups (n = 3), followed by tail-vein injection of free DOX and Fe_3O_4/DOX@CNSs with doses of 3mg/kg. Blood sample (0.3 mL) was taken from the eye socket of the SD rats at different times (0.17, 0.25, 0.5, 1, 2, 4, 8, 24 h) followed by a high-speed cryogenic centrifugation (15,000 rpm, 10 min). Plasma proteins were removed by methanol precipitation, and the concentrations of DOX were gauged by HPLC.

In vitro and vivo Antitumor Efficiency of Chemo-PTT

A chemo-PTT experiment was performed by using double Hoechst/propidium iodide (PI) staining. The 4T1 cells were seeded into 24-well plates, where a cell slide was placed to let the cells adhere. The cells were divided into 5 groups: NS with control group, DOX group, NIR group, Fe_3O_4@CNSs + NIR group, and Fe_3O_4/DOX@CNSs + NIR group (4 mg Fe/kg, DOX 200 μg/mL). The cells in groups NIR, Fe_3O_4@CNSs + NIR, and Fe_3O_4/DOX@CNSs + NIR were irradiated with an 808 nm laser (1.5 W/cm^2) for 10 min and incubated in a constant-temperature incubator for 1 h. Hoechst 33342 and PI dyes were added successively in the 24-well plates. In dark conditions, the cell slides were picked out with the needle tip of a syringe, and the cells with apoptosis and death were photographed using a biological microscope.

The tumor sizes were measured and calculated as volume = (tumor length) × (tumor width)^2/2. When the tumor volume of 4T1 tumor-bearing mice increased to approximately 150–200 mm^3, the mice were randomly divided into 5 groups (5 tumor-bearing mice per group): the grouping criteria were as above. Twenty-four hours after the tail vein injection of Fe_3O_4@CNSs and Fe_3O_4/DOX@CNSs, mice from groups NIR group, Fe_3O_4@CNSs + NIR group, and Fe_3O_4/DOX@CNSs + NIR were irradiated with an 808 nm laser (1.5 W/cm^2) for 10 min, once every 2 days, over a total of 14 days. The tumors were measured every 2 days over the 14-day period, and the changes in the tumor volume were observed. The mice in each group were euthanized according to standard animal protocols every 2 days, following which the tumors were removed and further hematoxylin and eosin (H&E) and terminal deoxynucleotidyl transferase dUTP nick end labeling (TUNEL) staining were performed for histological examination. During the above different treatment methods, the body weight of mice was recorded every 2 days.

Statistical Analysis

All the data were analyzed by SPSS 19.0 statistical software (SPSS, Inc., Chicago, IL, USA). Independent-sample *t*-test, paired-sample *t*-test, and analysis of variance were used to compare the differences between study groups. *P* value <0.05 was considered statistically significant.

Results and Discussion

Preparation and Characterization

Tumor-associated multifunctional theragnostic nanoplatforms have been in high demand in recent years for effective cancer therapy.[35] Herein, a low-toxicity multifunctional nanosystem, Fe_3O_4/DOX@CNSs, integrating chemo-PTT anti-tumor therapy and MRI monitoring, was successfully fabricated, and developed. In this synergistic anticancer therapy nanosystem, as illustrated in Figure 1, every part plays its own roles: CNSs guarantees excellent Fe_3O_4 and DOX loading, the CNSs and Fe_3O_4 provide NIR photothermal conversion efficiency, the decorated Fe_3O_4 facilitate Fe_3O_4 /DOX@CNSs NPs for T2 enhanced MR imaging. In our previous study, we utilized CNS derived from glucose as the tumor cell-targeting template to load a low dose of manganese oxide and first report of a saccharide-based magnetic NP with long-circulation, self-sacrificial and tumor-targeting capabilities. CNS possesses the intrinsic biological characteristics of saccharide derivatives, including high biosafety, reticuloendothelial system (RES) escape and tumor targeting, long-circulation, intracellular self-degradation, and excellent stability.[36] Therefore, in our study, we utilized a CNS derived from glucose as the tumor cell-targeting template to load the DOX and Fe_3O_4.

The surface morphology features of the CNSs (Figure S1) and Fe_3O_4@CNSs (Figure 2a) were observed by TEM. The CNSs were capped with foreign balls, which suggested that Fe_3O_4 was successfully loaded on the surface of the CNSs. The TEM, SEM and AFM of Fe_3O_4/DOX@CNSs were also obtained in Figure S2, and the smaller particles represent the Fe_3O_4. By comparing with the TEM of Fe_3O_4@CNSs, the TEM of Fe_3O_4/DOX@CNSs is almost unchanged. This is mainly because DOX is a molecule, which is difficult to cause the morphology change of nanomaterials. The XRD patterns of the prepared CNSs and Fe_3O_4@CNSs are shown in Figure 2b. The diffraction peaks of the CNSs and Fe_3O_4@CNSs are located at ~22°, indicating that the caramelized nanospheres are in an amorphous state.[24,37] The XRD peaks of the Fe_3O_4@CNSs can be indexed to the cubic phase [space group: Fd-3m (227)] of Fe_3O_4 (JCPDS card no. 19-0629), suggesting that Fe_3O_4 NPs are loaded on the surface of the caramelized nanospheres. The magnetic hysteresis loops of Fe_3O_4 and Fe_3O_4@CNSs are shown in Figure 2c. The saturation magnetizations are 62.5 emu/g, and 44.6 emu/g, respectively, indicating

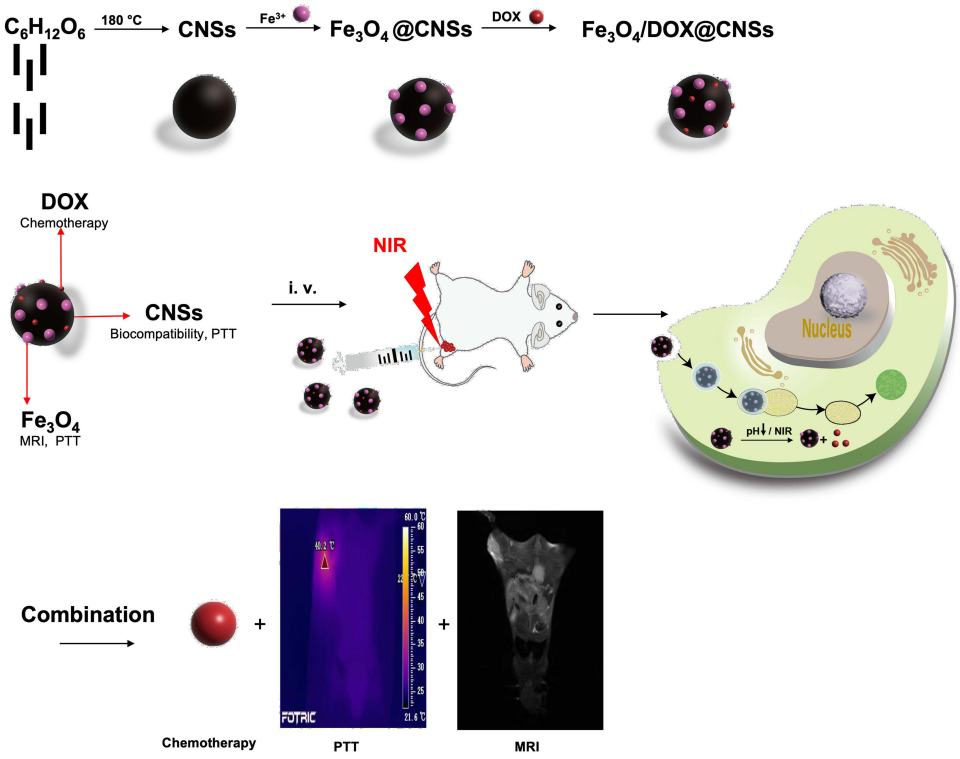

Figure 1 Schematic illustration of biocompatible and double-triggering Fe_3O_4/DOX@CNS nanosystem for combined chemo-PTT synergistic therapy and MR imaging monitoring.

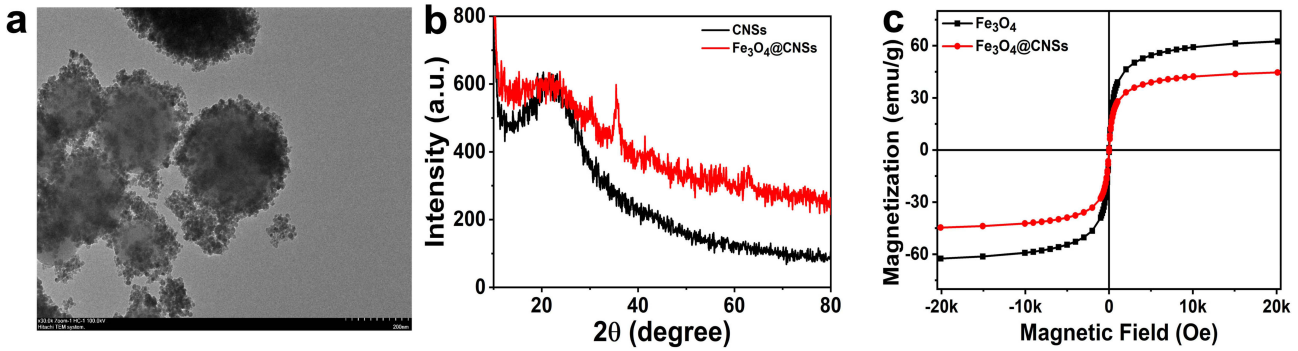

Figure 2 (**a**) TEM images of Fe_3O_4@CNSs. (**b**) XRD patterns of the CNSs and Fe_3O_4@CNSs. (**c**) Magnetic hysteresis loops and saturation magnetizations of Fe_3O_4 and Fe_3O_4@CNSs.

superparamagnetic. The Fe_3O_4@CNSs have a lower saturation magnetization than Fe_3O_4, which could be explained by the coating of Fe_3O_4 NPs on the CNSs. The loading of Fe_3O_4 on CNSs is determined to be 606.6 mg/g.

Drug Loading and Release Capacity of Fe_3O_4/DOX@CNSs

The surface zeta potential of the Fe_3O_4@CNSs and Fe_3O_4/DOX@CNSs changed from −29.2 mV to −27.5 mV after DOX conjugation (Figure 3a). Fourier transform infrared (FTIR) spectroscopy was used to identify the structure and functional groups of the CNSs, Fe_3O_4@CNSs and Fe_3O_4/DOX@CNSs (Figure 3b). The peak of the FTIR spectra at 580 cm-1 is attributed to the Fe–O stretching vibration. The peaks of CNSs, Fe_3O_4@CNSs and Fe_3O_4/DOX@CNSs at ~1704 cm-1 and 1625 cm-1 are assigned to C=O and C=C groups, respectively, which are formed by the caramelization of glucose.[38] The bands at ~3500 cm^{-1} indicate –OH stretching, and those in the 1000–1300 cm^{-1} range for –OH bending vibrations indicate the amount of –OH on the surface of the CNSs and Fe_3O_4@CNSs, which would improve the hydrophilicity of the NPs.[24]

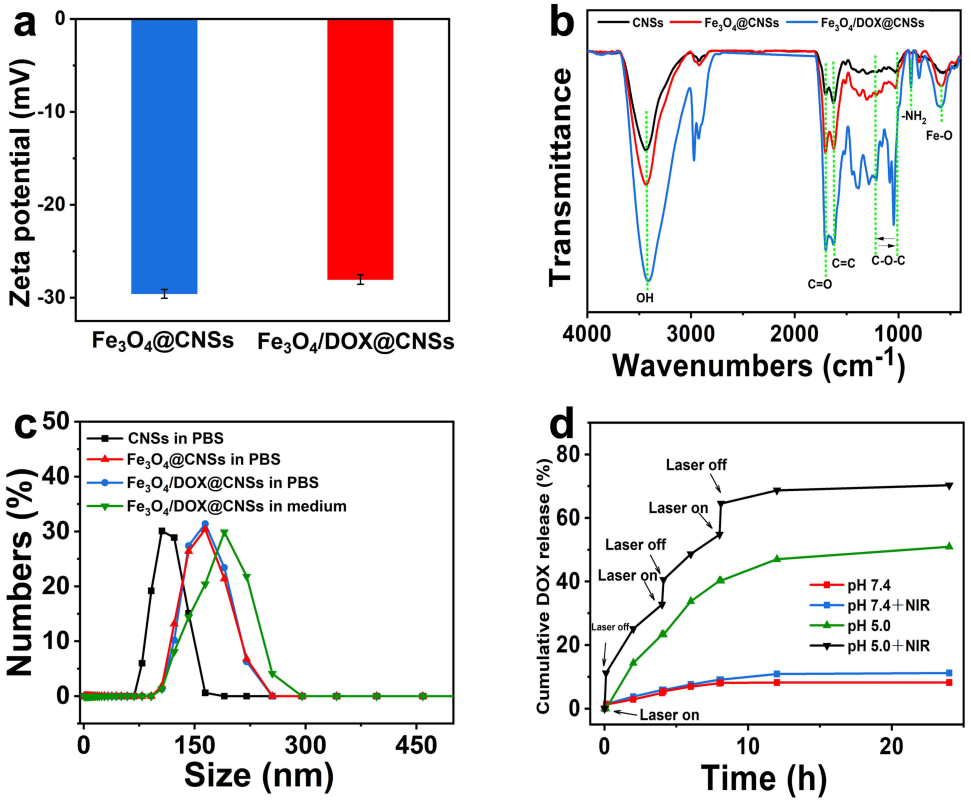

Figure 3 (**a**) Zeta potential of Fe_3O_4@CNSs, and Fe_3O_4/DOX@CNSs. (**b**) FTIR spectra of CNSs, Fe_3O_4@CNSs, and Fe_3O_4/DOX@CNSs. (**c**) Sizes of CNSs and Fe_3O_4 /DOX@CNSs. (**d**) Induced release of DOX from Fe_3O_4/DOX@CNSs under various pH levels (pH=7.4 and 5.0) and NIR irradiation.

Furthermore, compared to CNSs and Fe_3O_4@CNSs the FTIR spectra of the Fe_3O_4/DOX@CNSs (Figure 3b) show a mew peak at 877 cm^{-1}, which is assigned to $–NH_2$. In order to verify the connection mode of DOX with Fe_3O_4@CNSs, XPS analysis was carried out and no amide bond was found[39] from the Figure S3. In addition, there was no peak located at around 1230 cm^{-1} from IR spectrum of Fe_3O_4/DOX@CNSs in Figure 3b, suggesting no C=ONH was formed.[40] The loading of DOX on Fe3O4@CNSs may be mainly dependent on adsorption or incorporation because of the surface of Fe_3O_4@CNSs is negative charged while DOX is positive charged. Compared to Fe_3O_4@CNSs, the surface potential of Fe_3O_4/DOX@CNSs decreased to −28.0 mV due to the positive charge DOX. Additionally, the zeta potentials of the Fe3O4@CNSs and Fe_3O_4/DOX@CNSs were higher than 25 mV. According to DLVO theory, the zeta potential beyond ± 25 mV is stable because of their electrostatic repulsion, thus preventing agglomeration.[47] However, the negative charge carriers are beneficial in transdermal and lymphatic drug delivery but reduced cellular uptake compared to positive charge carriers.[41] The surface zeta potentials and FTIR spectra indicate that the Fe_3O_4@CNSs are successfully loaded with DOX.[42] The weight of DOX in the Fe_3O_4/DOX@CNSs was 29.8 mg/g. Additionally, the zeta potentials of the Fe_3O_4@CNSs and Fe_3O_4/DOX@CNSs were higher than 20 mV.

The average hydrodynamic diameters of the CNSs and Fe_3O_4/DOX@CNSs were determined by dynamic light scattering (DLS) (Figure 3c). This confirmed that the Fe_3O_4/DOX@CNSs had the same dispersibility in colloidal solutions, as well as cell culture medium and had very little aggregation, rendering the method suitable for drug delivery applications.[43] The results can be ascribed to the surface charge of Fe_3O_4/DOX@CNSs. The average sizes of the CNSs, Fe_3O_4@CNSs and Fe_3O_4/DOX@CNSs were in the range of 150 nm–180 nm (Figure 3c) with the polydispersity index (PDI) of 0.156, 0.354 and 0.358, respectively. The vascular endothelial cell gap at the tumor site can be around 100–780 nm, so nano-sized particles can enter the tissue through the vascular gap at the lesion, and when the NPs are loaded with drugs, it can achieve the greatest degree of blood circulation in solid tumors. Drug enrichment to achieve good therapeutic effect. NPs with a diameter in the range of 100–200 nm can better pass through the tumor enhanced permeability and retention (EPR) effect and escape the filtration of the liver and spleen.[44,45] Our Fe_3O_4/DOX@CNSs

has an average diameter of 150–180 nm, so it can better pass through the tumor EPR effect and effectively enrichment by tumor cells.

To evaluate the loading capacity of DOX in the nanocarrier, we carried out drug release detection experiments. The in vitro DOX release profiles of the Fe_3O_4/DOX@CNSs are pH/NIR-dependent (Figure 3d). Less than 10% of DOX is released at pH = 7.4 over 24 h, indicating relative stability under physiological conditions. The total drug release amount of the Fe_3O_4/DOX@CNSs in PBS solution (pH = 5) is 50.9%. Rapid drug release is observed under the 808 nm laser in the PBS solution (pH = 5), and a total drug release amount of 70.3% is obtained. This pH-responsive drug release is mainly attributed to two aspects: 1) Fe_3O_4 could fall off the surface of CNS and dissolve at pH = 5, so DOX adsorbed to Fe_3O_4 could release gradually; 2) The hydrophilicity and higher solubility of DOX increased in low-pH environments, which is caused by the increased number of protonated $–NH_2$ groups in DOX.[46] At the same time, the TEM of Fe_3O_4 /DOX@CNSs after it was placed in PBS solution (pH = 5) for 24 h, demonstrating Fe_3O_4 could dissolve (Figure S4). For in vivo bio applications, this pH-responsive DOX release could ensure that the Fe_3O_4/DOX@CNS nanocomposites remain stable in the physiological environment (pH = 7.4). Additionally, the enhanced drug release upon NIR irradiation can be attributed to the increasing temperature generated by Fe_3O_4/DOX@CNSs, which could directly increase the speed of desorption or release of DOX molecules for effective anticancer chemotherapy.[47]

Cytotoxicity of Fe_3O_4@CNSs and the in vitro Combined Chemo-PTT Therapy

Some studies have shown that nanomaterials such as those based on cashmere and copper sulfide can convert light into heat energy, leading to thermal damage, and are also quite toxic.[48,49] According to our previous research, CNSs and Mn-loaded CNSs show low toxicity, and are a highly biocompatible nanomaterial for diagnostic imaging and therapy.[24,43,50] However, the neurotoxicity of Mn limits its clinical translation.[24] Fe_3O_4, as a clinically safe nanomaterial, has good biocompatibility.[36,51] Therefore, we loaded Fe_3O_4 and DOX on CNSs and determined the cytotoxicity to investigate the safety of Fe_3O_4@CNSs and Fe_3O_4/DOX@CNSs. MCF-10A and 4T1 cells were cultured with different concentrations of Fe_3O_4@CNSs (0, 50, 100, 150, and 200 μg/mL) for different incubation times (12, 24, 36, and 48 h) and the standard cell survival rates were measured by CCK-8. The MCF-10A cells showed high cell survival rates. Even when the MCF-10A and 4T1 cells were cultured with Fe_3O_4@CNSs for 48 h at a concentration of 200 μg/mL, the cell vitality was more than 85% (Figure 4a and b).

The cytotoxic effect of Fe_3O_4/DOX@CNSs on 4T1 cells under NIR light irradiation was investigated by CCK-8 tests. In vitro cytotoxicity of each group after treatment with Fe_3O_4@CNSs, Fe_3O_4@CNSs+NIR, Fe_3O_4/DOX@CNSs, pure DOX and Fe_3O_4/DOX@CNSs + NIR for 24 h respectively, the evaluation was carried out and the results are shown in Figure 4c. The cells treated with Fe_3O_4@CNSs alone exhibited no significant cell death for all concentrations. The cells incubated with Fe_3O_4@CNSs + NIR exhibited moderate cell death, with almost 63% of the cells still viable up to a concentration of 200 μg/mL. The Fe_3O_4/DOX@CNSs had comparable cytotoxicity compared with pure DOX, indicating that the DOX-loaded CNS was pharmacologically active as a potential drug carrier. Cells cultured with Fe_3O_4/DOX@CNSs and exposed to laser irradiation for 10 minutes had a much higher number of deaths than any of the above, with less than 30% surviving cells at 200 μg/mL. The increased cell ablation could contribute to better therapeutic effects in combined chemo-PTT.

Hemolysis Rates, Quantitative Cellular Uptake and MRI Monitoring Capability of Fe_3O_4/DOX@CNSs

The absorbance value of each group at 545 nm was used to calculate the HR of Fe_3O_4/DOX@CNSs at different concentrations (10, 50, 100, 200 μg/mL) which were ranged from 0.79% to 1.95% (Table S1), far less than 5.0%. There was almost no hemolysis in the nanomaterials of different concentrations (Figure S5). Thus, the Fe_3O_4/DOX@CNSs had no hemolysis effect and conforms to the hemolysis requirement for medical materials.

The pre- and post-intake Fe contents were 4.60 ± 0.08 and 4.87 ± 0.19 pg for MCF-10A; 2.67 ± 0.55 and 4.89 ± 1.41 pg for macrophages; 4.22 ± 0.14 and 8.70 ± 0.91 pg for 4T1, respectively. No difference was observed between the pre- and post-uptake of Fe_3O_4/DOX@CNSs in MCF-10A cells (p=0.08). However, differences were noted between the pre- and post-uptake in 4T1 (p<0.01) and macrophages (p=0.04) (Figure 5a). This indicates that MCF-10A had limited uptake

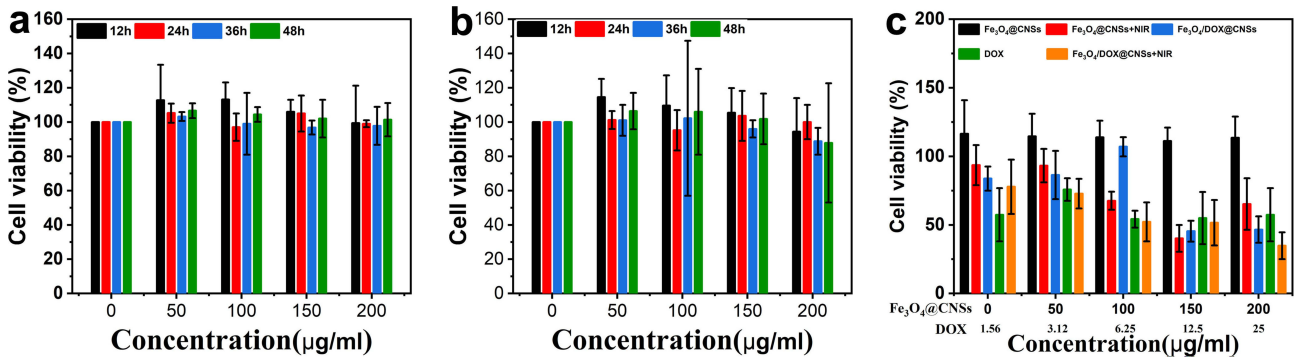

Figure 4 MCF-10A (**a**) and 4T1 (**b**) cell lines incubated with Fe_3O_4@CNSs at different concentrations (0, 50, 100, 150, and 200 μg/mL) for various durations (12, 24, 36, and 48 h). (**c**) In vitro cytotoxicity of Fe_3O_4@CNSs, Fe_3O_4@CNSs + NIR, Fe_3O_4/DOX@CNSs, pure DOX, and Fe_3O_4/DOX@CNSs + NIR against 4T1 cells after 24 h of incubation.

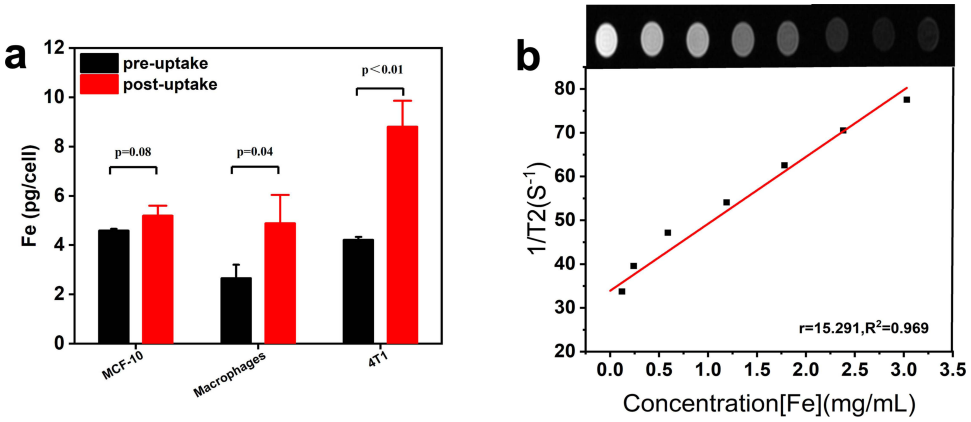

Figure 5 (**a**) Cellular pre- and post-uptake of Fe_3O_4/DOX@CNSs by MCF-10A, macrophages and 4T1 cells. (**b**) Linear relationship of r^2 (1/T2) values vs concentration of Fe_3O_4/DOX@CNSs.

of Fe_3O_4/DOX@CNSs compared with human macrophages and 4T1 cells. The possible reason was that CNSs were obtained through caramelization reaction of anhydrous glucose.[52] The expression of glucose transporter (Glut1) receptor is increased in breast cancer. We speculated that the uptake of Fe_3O_4/DOX@CNSs is related to the expression of more Glut1 on the surface of tumor cell membranes to meet its growing energy demands.[53,54] Compared with tumor cells, there are fewer glucose transporter receptors on the surface of MCF-10A. Therefore, there is less uptake of Fe_3O_4 /DOX@CNSs than 4T1. Moreover, the average size of Fe_3O_4/DOX@CNSs is 150 nm–180 nm, while particles of 200 nm or greater in size are more efficiently taken up by the reticuloendothelial system (RES) rich in macrophages.[55–57] So Fe_3O_4/DOX@CNSs could partly avoid amounts of uptake by RES.

The Fe_3O_4/DOX@CNSs mainly affected the relaxation time of the T2 image, which had a small effect on the T1 image and could achieve a negative enhancement effect. As shown in Figure 5b, the T2 images become dark gradually as the concentration of the Fe_3O_4/DOX@CNSs increase. Additionally, in comparison to the previous reported,[35] the r value of the Fe_3O_4/DOX@CNSs can reach 15.291 $(mg/mL)^{-1}S^{-1}$, and we have similar R^2 values. This indicates that the synthesized material has a better ability to shorten T2. This might be due to that Fe_3O_4/DOX@CNSs could provide the advantages of proper size and shape, which can increase the chance of improving the rate of relaxation rates and the ideal modification of the contrast agent label.[58]

Vitro and vivo Photothermal Effect of Fe_3O_4/DOX@CNSs

Typically, cancer cells are more sensitive to heat than normal cells due to the immature vasculature structure. Many studies have reported that cancer cells can be killed by being kept at 42°C for 15–60 min or only 4–6 min when the

temperature exceeds 50°C.[59,60] However, high temperatures (52°C) cause irreversible damage to normal cells.[61] Thus, mild PTT is a promising cancer treatment for the minimal damage to the normal cells.

The Fe_3O_4/DOX@CNSs aqueous solution has a wide absorption range (400–1000 nm) from visible light to near-infrared light (Figure S6). This shows that Fe_3O_4/DOX@CNSs have the theoretical basis for near-infrared photothermal conversion.[38] The photothermal conversion of Fe_3O_4/DOX@CNSs in aqueous solution was achieved by irradiation with NIR (808 nm, 1.5 W/cm^2). With the extension of irradiation time (0, 120, 240, 360, 480 s) and the increase in Fe_3O_4 /DOX@CNSs solution concentration (100, 200, 400, 600 μg/mL), the temperature of the Fe_3O_4@CNSs solution increased significantly (Figure 6a), and corresponding temperature curve is shown in Figure S7. Fe_3O_4/DOX@CNSs (0 and 100 μg/mL) solutions show minimal temperature change (rising to 37°C and 41°C, respectively) after 5 min of irradiation. The temperature of 200 μg/mL Fe_3O_4@CNSs increased to 45°C, which is sufficient to destroy tumor cells.[8] The 400 μg/mL and 600 μg/mL Fe_3O_4/DOX@CNSs solution temperatures reached 50°C and 56°C, respectively, after 5 min of irradiation. To further analyze the photothermal stability of Fe_3O_4@CNSs, a near-infrared laser (808 nm, 1.5 W/cm^2) irradiated 100 μg/mL Fe_3O_4/DOX@CNSs for 5 min, which was then cooled to room temperature and then further irradiated for 5 min for a total of ten cycles (ie, 100 min irradiation). The results showed that the photothermal conversion ability of Fe_3O_4 /DOX@CNSs did not decrease after ten cycles (Figure 6b). This indicates that Fe_3O_4/DOX@CNSs have good photothermal conversion efficiency and stability and show good potential as a photothermal agent.

The photothermal effect of Fe_3O_4/DOX@CNSs was excellent in vitro, and we further explored the feasibility of Fe_3O_4/DOX@CNSs as a photothermal agent to treat tumors in vivo. Tumor-bearing mice were injected into the tail vein with CNSs and Fe_3O_4/DOX@CNSs (4 mg Fe/kg, 3 mice per group). An 808 nm laser (1.5 W/cm^2) was used for 10 min of irradiation, and the temperature change was observed (Figure 6c and d). In the NS group, the temperature in the tumor areas was raised to 41.5°C, however, a rapid temperature increase from 29.3°C to 60.8°C was observed for tumors in the Fe_3O_4/DOX@CNSs group.[62] Under the same irradiation conditions, the tumor temperature of mice injected with NS was

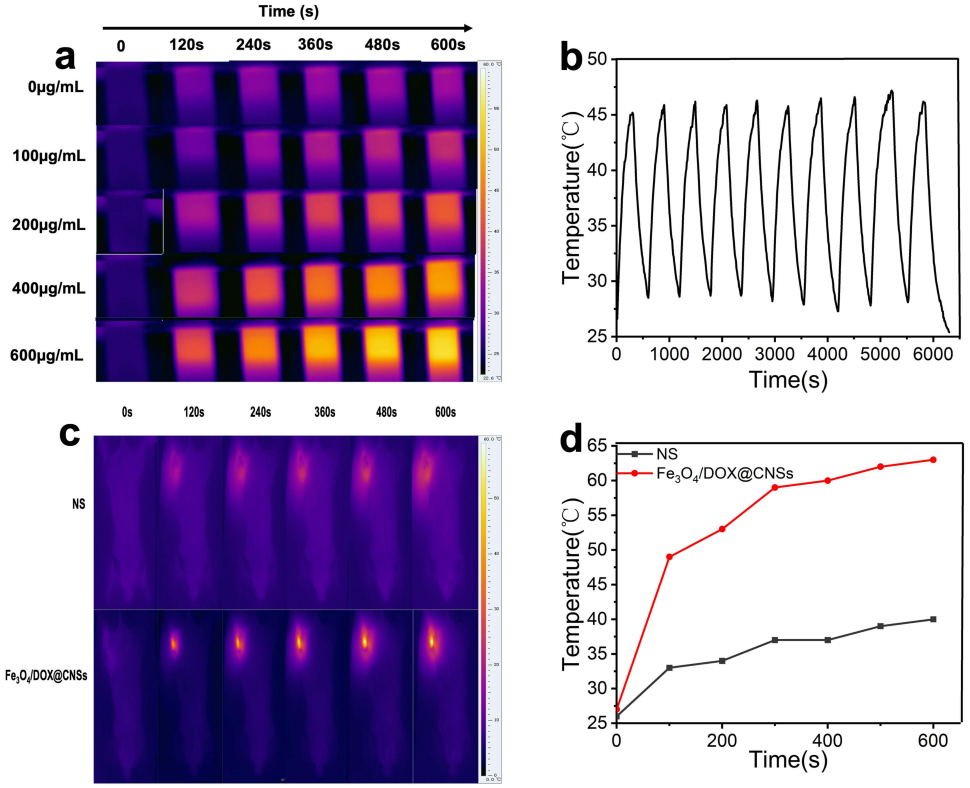

Figure 6 (**a**) Infrared thermal images of NS and Fe_3O_4/DOX@CNSs. (**b**) The temperature change of Fe_3O_4/DOX@CNSs solution (100 mg/mL) after turning cycling the laser four times. (**c**) Thermographs of the tumor region after intravenous injection with NS and Fe_3O_4/DOX@CNSs. (**d**) Heating curve of the various groups.

significantly lower than that of Fe_3O_4/DOX@CNSs. This shows that Fe_3O_4/DOX@CNSs have a relatively efficient thermal effect and could be used as a PTT agent for in vivo tumor ablation.

In vivo MRI Imaging of Fe_3O_4/DOX@CNSs

In recent years, many researchers have focused on assisted NIR nanocarriers with imaging monitoring for precise cancer diagnosis and location in order to guide external laser irradiation without damaging the surrounding healthy tissue.[63] We further studied the in vivo MRI performance of Fe_3O_4/DOX@CNSs. The in vivo MR imaging was performed on 4T1 tumor-bearing BABL/c mice after intravenous injection of 0.1 mL Fe_3O_4/DOX@CNSs (4 mg Fe/kg) and scanned with a 3.0 T MRI scanner. Figure 7 shows MR images of mouse tumors (red circles) at different time intervals. The T2 signal intensity changed in the tumor after injection of Fe_3O_4/DOX@CNSs (Figure S8). Within 24 h after Fe_3O_4/DOX@CNSs injection, the T2 signal intensity in the tumor gradually decreased. During this period, the overall background signal intensity of the mice also gradually decreased, and after 24 h, the T2 signal intensity of tumor gradually increased. Thus, the Fe_3O_4@CNSs could help to integrate both MRI monitoring and chemo-PTT into a single multimodal nanosystem to construct a theragnostic platform, which can help to diagnose and locate the cancer and to visualize NP accumulation.

In vivo Blood Circulation of Fe_3O_4/DOX@CNSs and Clearance of Fe_3O_4 /DOX@CNSs

In Figure 8a, the blood concentration of Fe^{3+} decreases gradually and is retained for more than 24 h, it was confirmed that Fe_3O_4/DOX@CNSs has a long blood circulation, which can delay the clearance of NPs by macrophages in the reticuloendothelial system[64] and is more beneficial to the large uptake of Fe_3O_4/DOX@CNSs by tumor tissue through EPR effect. This is consistent with the lowest T2 signal intensity of the tumor tissue 24 h after the tail vein injection of Fe_3O_4/DOX@CNSs in 4T1 tumor-bearing mice. Figure 8b shows that Fe^{3+} accumulates in most organs (heart, liver, spleen, kidney, and lungs), while the tumor exhibits the most Fe^{3+} uptake. The tumor uptake of Fe^{3+} which can be associated with the EPR effect. In addition, as mentioned above, 4T1 cells that express a large amount of Glut on the

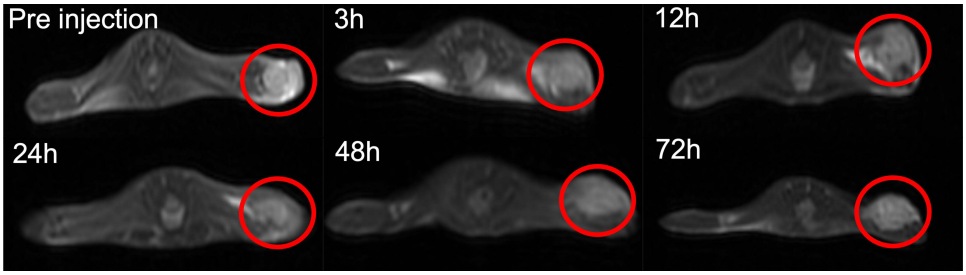

Figure 7 In vivo T2 MRI of 4T1 tumor-bearing mice at different time intervals (0, 3, 12, 24, 48 and 72 h) after injection with Fe_3O_4/DOX@CNSs (4 mg Fe/kg).

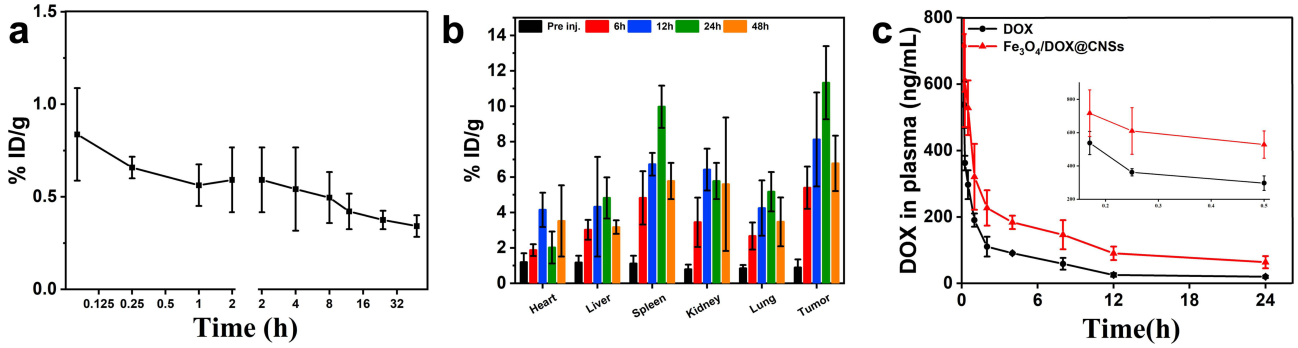

Figure 8 (**a**) Blood circulation and (**b**) biodistribution of Fe_3O_4/DOX@CNSs observed after intravenous injection in mice. Fe concentration measurements were performed by ICP- MS. (**c**) Pharmacokinetic of free DOX and Fe_3O_4/DOX@CNSs after a single dosage intravenous to rat.

surface contribute to the uptake large amounts of glucose. We can also find kidney tissues accumulated much more Fe^{3+}. The kidney uptake of Fe^{3+} can be contributed to possible renal excretion.[65]

In vivo Pharmacokinetics Study

The pharmacokinetics behavior of DOX was studied in rats through the tail-vein injection of free DOX and Fe_3O_4 /DOX@CNSs. The concentration of DOX in plasma at different times is shown in Figure 8c. Compared with free DOX, the pharmacokinetic characteristics of Fe_3O_4/DOX@CNSs in vivo were significantly changed based on the pharmacokinetic parameters of the two groups as presented in Table 1. At the same dose, the elimination half-life time (t1/2β) of DOX in Fe_3O_4/DOX@CNSs group was significantly increased by 11.18h compared with free DOX group. The clearance rate (CL) of free DOX group was 2.61 times as much as Fe_3O_4/DOX@CNSs group, respectively. The decreases of in vivo CL in Fe_3O_4/DOX@CNSs group might be due to the increased blood stability by escaping the RES and the sustained release of DOX from NPs. In addition, the mean retention time (MRT), area under the curve $AUC_{0\rightarrow t}$ and $AUC_{0\rightarrow \infty}$ values of Fe_3O_4/DOX@CNSs group were significantly increased by 0.51, 1.31 and 1.65 -fold, respectively, compared with free DOX group. These results demonstrated that Fe_3O_4/DOX@CNSs with a sustained release property could significantly improve the bioavailability of DOX.[66]

Vitro and vivo Therapeutic Efficacy of Chemo-Photothermal Treatment

Segy et al[67] and many others have shown that combining Fe_3O_4 with PTT allows diagnosis and treatment; however, the studies of these researchers did not combine photothermal treatment with chemotherapy to achieve a combined therapeutic effect.[32,68] Here, we combined the two treatments and verified their effect. Since CNSs and Fe_3O_4 have been proven to have photothermal effects, no separate group was required.[43,51]

To confirm the efficacy of Fe_3O_4@CNSs PTT combined with DOX in the treatment of tumors, 4T1 cells (including living, apoptotic, and dead cells) were stained with Hoechst 33342 and PI (Figure 9a). The survival rate of the control group was up to 99%. The DOX group showed a few dead cells. The NIR and Fe_3O_4@CNSs + NIR groups showed partial dead cells, but Fe_3O_4@CNSs + NIR showed greater potential for killing cells. Hence, Fe_3O_4@CNSs have photothermal superposition ability, rendering PTT an effective strategy for tumors. When tumor cells were exposed to DOX combined with Fe_3O_4@CNSs and subjected to laser irradiation almost all cells died, indicating that DOX combined with PTT could effectively induce cell death and achieve effective treatment.

Over 14 days, the tumor volume of the control group increased by 12.8 times, that of the DOX group increased by 10.4 times, and that of the NIR group increased by 7.5 times, indicating that, compared with chemotherapy, NIR has the highest potential to kill tumor cells. The traditional chemotherapy drug, DOX, also influenced the tumor volume. However, DOX has known toxicity. After 10 days of DOX injection, the mice were in poor health, and some even died. Fourteen days after Fe_3O_4@CNSs + NIR treatment, the tumor volume increased by 2.3 times; after 14 days of Fe_3O_4/DOX@CNSs + NIR treatment, the tumor volume decreased by 32%. Thus, chemotherapy combined with PTT may effectively inhibit tumor growth and have better antitumor effects than either treatment alone (Figure 9b).

Table 1 Pharmacokinetic Parameters of DOX and Fe_3O_4/DOX@CNSs After a Single Dosage Intravenous to Rat

Pharmacokinetic Parameters	DOX	Fe_3O_4/DOX@CNSs
t1/2β (h)	5.71 ± 2.91	16.89 ± 4.35**
CL (L/h)	1.75 ± 0.09	0.67 ± 0.10***
MRT (h)	11.58 ± 2.65	17.52 ± 6.17*
$AUC_{0\rightarrow t}$ (μg·h/L)	1429.47 ± 47.22	3300.21 ± 56.60***
$AUC_{0\rightarrow \infty}$(μg·h/L)	1718.27 ± 89.64	4561.74 ± 739.96**

Notes: *$P < 0.05$, **$P < 0.01$, ***$P < 0.001$ versus free DOX treatment. Data were presented as mean ± SD (n=3).

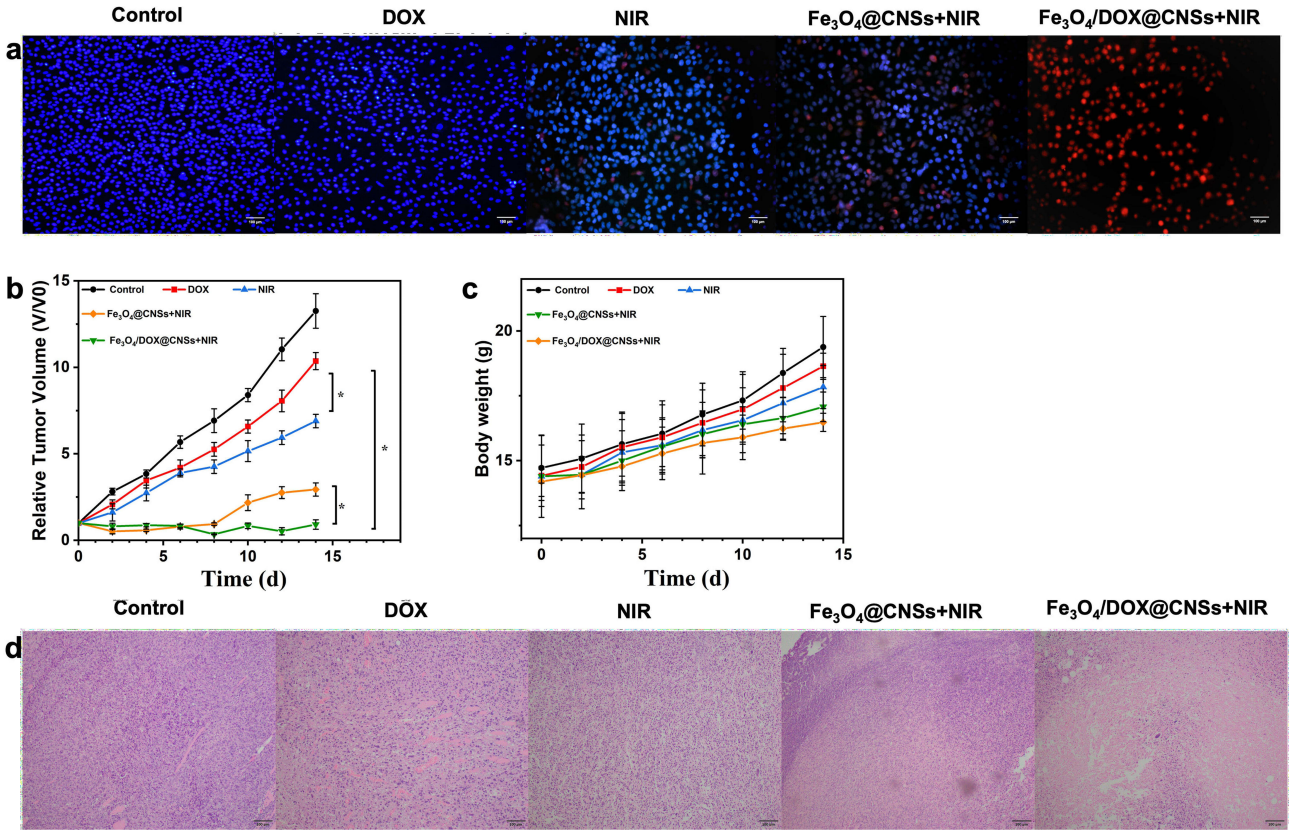

Figure 9 Hoechst 33342/PI fluorescence staining of 4T1 cells after different treatments with NS as control, DOX, NIR, Fe_3O_4@CNSs + NIR, and Fe_3O_4/DOX@CNSs + NIR, respectively (**a**), scale bar = 100 μm. The relative tumor volume (**b**) and body weights curves (**c**) of mice after different treatments (*p<0.05). H&E-stained images of tumors from different groups (**d**), scale bar = 100 μm.

Additionally, all mice remained healthy, suggesting that the mice were neither starving nor diseased.[69] During the experiments, the body weights and tumor volumes of mice were monitored every two days and the results are recorded in Figure S9. The variation trends of the mean body weights (Figure 9c) show that the weights of mice in all seven groups increased with a similar increase trend. However, the weight gain of mice in Fe_3O_4/DOX@CNSs + NIR group was the slowest, which may be related to its effective therapeutic effect. The tumors of the different groups were analyzed histologically and stained with H&E and TUNEL. After staining, the nuclei of the control group were large, dark, and dense, without distinct damage. The DOX group had a few abnormal and dead cells. The Fe_3O_4@CNSs + NIR group exhibited necrosis, the tumor cells had lost their cell morphology, and there was evidence of lamellar necrosis. In the Fe_3O_4/DOX@CNSs + NIR group, massive necrosis was evident, and features related to necrosis could be clearly observed, such as cytoskeleton and nuclear disintegration (Figure 9d, Figure S10).

Organ histology (Figure S11) of the mice was performed to exclude the possibility of induced toxicity. Serious irreversible pathological alterations and injuries to the organs of mice in all groups were eliminated through H&E analysis, demonstrating the safety of Fe_3O_4/DOX@CNSs during medicating photothermal and chemical ablations. Therefore, Fe_3O_4/DOX@CNSs could act as a powerful chemo-PTT agent in vivo.

Conclusion

In this work, the multifunctional nanosystem of Fe_3O_4/DOX@CNSs could simultaneously achieve NIR-responsive chemo-PTT and MRI monitoring to enhance the therapeutic efficacy for TNBC. In vivo, Fe_3O_4/DOX@CNSs had longer circulation with higher AUC compared with DOX. The photothermal effect of Fe_3O_4/DOX@CNSs under 808 nm irradiation can not only rapidly heat up tumor tissue and "cook" cancer cells, but also promote the release of DOX, thereby providing synergy for 4T1 cells in vitro. Pathological results showed that the heart, lung, kidney; liver, spleen

and other organs had no obvious lesions. In summary, the system has the properties of easy synthesis, good biocompatibility, and low toxicity. The effective monitoring of MRI and the effect of combined chemo-PTT therapy will provide a new way for the treatment of TNBC.

Acknowledgment

This research was supported by the National Natural Science Foundation of China (NSFC81771888).

Disclosure

The authors declare no competing financial interest.

References

1. Wilkinson L, Gathani T. Understanding breast cancer as a global health concern. *Br J Radiol*. 2022;95(1130):20211033. doi:10.1259/bjr.20211033
2. Xiao Y, Ma D, Yang YS, et al. Comprehensive metabolomics expands precision medicine for triple-negative breast cancer. *Cell Res*. 2022;32(5):477–490. doi:10.1038/s41422-022-00614-0
3. Al-Mahmood S, Sapiezynski J, Garbuzenko OB, Minko T. Metastatic and triple-negative breast cancer: challenges and treatment options. *Drug Deliv Transl Res*. 2018;8(5):1483–1507. doi:10.1007/s13346-018-0551-3
4. Lee KL, Kuo YC, Ho YS, Huang YH. Triple-negative breast cancer: current understanding and future therapeutic breakthrough targeting cancer stemness. *Cancers*. 2019;11(9):1334. doi:10.3390/cancers11091334
5. Matsen CB, Neumayer LA. Breast cancer: a review for the general surgeon. *JAMA Surg*. 2013;148(10):971–979. doi:10.1001/jamasurg.2013.3393
6. Maughan KL, Lutterbie MA, Ham PS. Treatment of breast cancer. *Am Fam Physician*. 2010;81(11):1339–1346.
7. Oh Y, Jin JO, Oh J. Photothermal-triggered control of sub-cellular drug accumulation using doxorubicin-loaded single-walled carbon nanotubes for the effective killing of human breast cancer cells. *Nanotechnology*. 2017;28(12):125101. doi:10.1088/1361-6528/aa5d7d
8. Fan X, Yuan Z, Shou C, et al. cRGD-conjugated Fe3O4@PDA-DOX multifunctional nanocomposites for MRI and antitumor chemo-photothermal therapy. *Int J Nanomedicine*. 2019;14:9631–9645. doi:10.2147/IJN.S222797
9. Suo A, Qian J, Zhang Y, Liu R, Xu W, Wang H. Comb-like amphiphilic polypeptide-based copolymer nanomicelles for co-delivery of doxorubicin and P-gp siRNA into MCF-7 cells. *Mater Sci Eng C Mater Biol Appl*. 2016;62:564–573. doi:10.1016/j.msec.2016.02.007
10. Shen S, Ding B, Zhang S, et al. Near-infrared light-responsive nanoparticles with thermosensitive yolk-shell structure for multimodal imaging and chemo-photothermal therapy of tumor. *Nanomedicine*. 2017;13(5):1607–1616. doi:10.1016/j.nano.2017.02.014
11. Yin L, Duan JJ, Bian XW, Yu SC. Triple-negative breast cancer molecular subtyping and treatment progress. *Breast Cancer Res*. 2020;22(1):61. doi:10.1186/s13058-020-01296-5
12. Forrai G, Kovács E, Ambrózay É, et al. Use of diagnostic imaging modalities in modern screening, diagnostics and management of breast tumours 1st central-eastern European professional consensus statement on breast cancer. *Pathol Oncol Res*. 2022;28:1610382. doi:10.3389/pore.2022.1610382
13. Mo T, Brandal SHB, Köhn-Luque A, et al. Quantification of tumor hypoxia through unsupervised modelling of consumption and supply hypoxia MR imaging in breast cancer. *Cancers*. 2022;14(5):1326. doi:10.3390/cancers14051326
14. Nian D, Shi P, Sun J, Ren L, Hao X, Han J. Application of luteinizing hormone-releasing hormone-ferrosoferric oxide nanoparticles in targeted imaging of breast tumors. *J Int Med Res*. 2019;47(4):1749–1757. doi:10.1177/0300060519834457
15. Chen Z, Wang Q, Wang H, et al. Ultrathin PEGylated W18O49 nanowires as a new 980 nm-laser-driven photothermal agent for efficient ablation of cancer cells in vivo. *Adv Mater*. 2013;25(14):2095–2100. doi:10.1002/adma.201204616
16. Melancon MP, Lu W, Zhong M, et al. Targeted multifunctional gold-based nanoshells for magnetic resonance-guided laser ablation of head and neck cancer. *Biomaterials*. 2011;32(30):7600–7608. doi:10.1016/j.biomaterials.2011.06.039
17. Khafaji M, Zamani M, Golizadeh M, Bavi O. Inorganic nanomaterials for chemo/photothermal therapy: a promising horizon on effective cancer treatment. *Biophys Rev*. 2019;11(3):335–352. doi:10.1007/s12551-019-00532-3
18. Shao F, Pan Z, Long Y, et al. Nectin-4-targeted immunoSPECT/CT imaging and photothermal therapy of triple-negative breast cancer. *J Nanobiotechnology*. 2022;20(1):243. doi:10.1186/s12951-022-01444-3
19. Mishra SK, Dhadve AC, Mal A, et al. Photothermal therapy (PTT) is an effective treatment measure against solid tumors which fails to respond conventional chemo/radiation therapies in clinic. *Biomater Adv*. 2022;143:213153. doi:10.1016/j.bioadv.2022.213153
20. Avila-Flores R, Medellin RA. Ecological, taxonomic, and physiological correlates of cave use by Mexican bats. *J Mammal*. 2004;85(4):675–687. doi:10.1644/Bos-127
21. Lambert TN, Andrews NL, Gerung H, et al. Water-soluble germanium(0) nanocrystals: cell recognition and near-infrared photothermal conversion properties. *Small*. 2007;3(4):691–699. doi:10.1002/smll.200600529
22. Huang X, Tang S, Liu B, Ren B, Zheng N. Enhancing the photothermal stability of plasmonic metal nanoplates by a core-shell architecture. *Adv Mater*. 2011;23(30):3420–3425. doi:10.1002/adma.201100905
23. Cheng L, Wang C, Feng L, Yang K, Liu Z. Functional nanomaterials for phototherapies of cancer. *Chem Rev*. 2014;114(21):10869–10939. doi:10.1021/cr400532z
24. Xiang Y, Li N, Guo L, et al. Biocompatible and pH-sensitive MnO-loaded carbonaceous nanospheres (MnO@CNSs): a theranostic agent for magnetic resonance imaging-guided photothermal therapy. *Carbon*. 2018;136:113–124. doi:10.1016/j.carbon.2018.04.058
25. Hong G, Diao S, Antaris AL, Dai H. Carbon nanomaterials for biological imaging and nanomedicinal therapy. *Chem Rev*. 2015;115(19):10816–10906. doi:10.1021/acs.chemrev.5b00008
26. Miao ZH, Wang H, Yang H, Li Z, Zhen L, Xu CY. Glucose-derived carbonaceous nanospheres for photoacoustic imaging and photothermal therapy. *ACS Appl Mater Interfaces*. 2016;8(25):15904–15910. doi:10.1021/acsami.6b03652

27. Wang Y, Li X, Chen P, Dong Y, Liang G, Yu Y. Enzyme-instructed self-aggregation of Fe3O4 nanoparticles for enhanced MRI T2 imaging and photothermal therapy of tumors. *Nanoscale*. 2020;12(3):1886–1893. doi:10.1039/c9nr09235h
28. Zhou Z, Huang D, Bao J, et al. A synergistically enhanced T(1) -T(2) dual-modal contrast agent. *Adv Mater*. 2012;24(46):6223–6228. doi:10.1002/adma.201203169
29. Lee N, Hyeon T. Designed synthesis of uniformly sized iron oxide nanoparticles for efficient magnetic resonance imaging contrast agents. *Chem Soc Rev*. 2012;41(7):2575–2589. doi:10.1039/c1cs15248c
30. Oh Y, Je JY, Moorthy MS, Seo H, Cho WH. pH and NIR-light-responsive magnetic iron oxide nanoparticles for mitochondria-mediated apoptotic cell death induced by chemo-photothermal therapy. *Int J Pharm*. 2017;531(1):1–13. doi:10.1016/j.ijpharm.2017.07.014
31. Zhang X, Xu X, Li T, et al. Composite photothermal platform of polypyrrole-enveloped Fe3O4 nanoparticle self-assembled superstructures. *ACS Appl Mater Interfaces*. 2014;6(16):14552–14561. doi:10.1021/am503831m
32. Ge R, Li X, Lin M, et al. Fe3O4@polydopamine composite theranostic superparticles employing preassembled Fe3O4 Nanoparticles as the core. *ACS Appl Mater Interfaces*. 2016;8(35):22942–22952. doi:10.1021/acsami.6b07997
33. Tao K, Liu S, Wang L, et al. Targeted multifunctional nanomaterials with MRI, chemotherapy and photothermal therapy for the diagnosis and treatment of bladder cancer. *Biomater Sci*. 2019;8:342–352. doi:10.1039/c9bm01377f
34. Yoon J, Cho SH, Seong H. Multifunctional ultrasmall superparamagnetic iron oxide nanoparticles as a theranostic agent. *Colloids Surfaces A*. 2017;520:892–902. doi:10.1016/j.colsurfa.2017.02.080
35. Liu B, Zhang X, Li C, et al. Magnetically targeted delivery of DOX loaded Cu9S5@mSiO2@Fe3O4-PEG nanocomposites for combined MR imaging and chemo/photothermal synergistic therapy. *Nanoscale*. 2016;8(25):12560–12569. doi:10.1039/c5nr06322a
36. Qi Y, Li W, Fang J, et al. Application and mechanism of manganese-coated caramelization nanospheres for active targeting in hepatobiliary tumors. *Nanomedicine*. 2019;14(22):2973–2985. doi:10.2217/nnm-2018-0272
37. Jin S, Deng H, Long D, et al. Facile synthesis of hierarchically structured Fe3O4/carbon micro-flowers and their application to lithium-ion battery anodes. *J Power Sources*. 2011;196(8):3887–3893. doi:10.1016/j.jpowsour.2010.12.078
38. Sun X, Li Y. Colloidal carbon spheres and their core/shell structures with noble-metal nanoparticles. *Angew Chem Int Ed Engl*. 2004;43(5):597–601. doi:10.1002/anie.200352386
39. Ostadhossein F, Vulugundam G, Misra SK, Srivastava I, Pan D. Chirality inversion on the carbon dot surface via covalent surface conjugation of cyclic α-amino acid capping agents. *Bioconjug Chem*. 2018;29(11):3913–3922. doi:10.1021/acs.bioconjchem.8b00736
40. Wei Y, Chen L, Wang J, Liu X, Yang Y, Yu S. Investigation on the chirality mechanism of chiral carbon quantum dots derived from tryptophan. *RSC Adv*. 2019;9(6):3208–3214. doi:10.1039/c8ra09649j
41. Finbloom JA, Sousa F, Stevens MM, Desai TA. Engineering the drug carrier biointerface to overcome biological barriers to drug delivery. *Adv Drug Deliv Rev*. 2020;167:89–108. doi:10.1016/j.addr.2020.06.007
42. Oladipo AO, Nkambule TTI, Mamba BB, Msagati TAM. The stimuli-responsive properties of doxorubicin adsorbed onto bimetallic Au@Pd nanodendrites and its potential application as drug delivery platform. *Mater Sci Eng C*. 2020;110. doi:10.1016/j.msec.2020.110696.
43. Guo W, Qi Y, Zhang Y, Ma L, Yu D, Zhan J. Biocompatible caramelized carbonaceous nanospheres supported paramagnetic ultrathin manganese oxide nanosheets via self-sacrificing reduction as a MRI contrast agent for liver imaging. *Carbon*. 2016;110:321–329. doi:10.1016/j.carbon.2016.09.030
44. Blanco E, Shen H, Ferrari M. Principles of nanoparticle design for overcoming biological barriers to drug delivery. *Nat Biotechnol*. 2015;33(9):941–951. doi:10.1038/nbt.3330
45. Sharifi M, Cho WC, Ansariesfahani A, et al. An updated review on EPR-based solid tumor targeting nanocarriers for cancer treatment. *Cancers*. 2022;14(12):2868. doi:10.3390/cancers14122868
46. Liu B, Li C, Yang D, et al. Whole-genome analyses resolve early branches in the tree of life of modern birds. *Science*. 2014. 2014:1906–1913.
47. Wu L, Wu M, Zeng Y, et al. Multifunctional PEG modified DOX loaded mesoporous silica nanoparticle@ CuS nanohybrids as photo-thermal agent and thermal-triggered drug release vehicle for hepatocellular carcinoma treatment. *Nanotechnology*. 2014;26(2):025102. doi:10.1088/0957-4484/26/2/025102
48. Lu N, Huang P, Fan W, et al. Tri-stimuli-responsive biodegradable theranostics for mild hyperthermia enhanced chemotherapy. *Biomaterials*. 2017;126:39–48. doi:10.1016/j.biomaterials.2017.02.025
49. Qin J, Peng Z, Li B, et al. Gold nanorods as a theranostic platform for in vitro and in vivo imaging and photothermal therapy of inflammatory macrophages. *Nanoscale*. 2015;7(33):13991–14001. doi:10.1039/c5nr02521d
50. Jamalipour Soufi G, Iravani S. Eco-friendly and sustainable synthesis of biocompatible nanomaterials for diagnostic imaging: current challenges and future perspectives. *Green Chem*. 2020;22(9):2662–2687. doi:10.1039/d0gc00734j
51. Zhou Z, Sun Y, Shen J, et al. Iron/iron oxide core/shell nanoparticles for magnetic targeting MRI and near-infrared photothermal therapy. *Biomaterials*. 2014;35(26):7470–7478. doi:10.1016/j.biomaterials.2014.04.063
52. Zhang X, Chen F, Wang M. Impacts of selected dietary polyphenols on caramelization in model systems. *Food Chem*. 2013;141(4):3451–3458. doi:10.1016/j.foodchem.2013.06.053
53. Yu L, Chen Y, Wu M, et al. "Manganese extraction" strategy enables tumor-sensitive biodegradability and theranostics of nanoparticles. *J Am Chem Soc*. 2016;138(31):9881–9894. doi:10.1021/jacs.6b04299
54. Pan D, Caruthers SD, Hu G, et al. Ligand-directed nanobialys as theranostic agent for drug delivery and manganese-based magnetic resonance imaging of vascular targets. *J Am Chem Soc*. 2008;130(29):9186–9187. doi:10.1021/ja801482d
55. Chang H, Yhee JY, Jang GH, et al. Predicting the in vivo accumulation of nanoparticles in tumor based on in vitro macrophage uptake and circulation in zebrafish. *J Control Release*. 2016;244(Pt B):205–213. doi:10.1016/j.jconrel.2016.07.025
56. Desai N. Challenges in development of nanoparticle-based therapeutics. *Aaps j*. 2012;14(2):282–295. doi:10.1208/s12248-012-9339-4
57. Gaumet M, Vargas A, Gurny R, Delie F. Nanoparticles for drug delivery: the need for precision in reporting particle size parameters. *Eur J Pharm Biopharm*. 2008;69(1):1–9. doi:10.1016/j.ejpb.2007.08.001
58. Zhang Q, Shan W, Ai C, et al. Construction of multifunctional Fe(3)O(4)-MTX@HBc nanoparticles for MR imaging and photothermal therapy/chemotherapy. *Nanotheranostics*. 2018;2(1):87–95. doi:10.7150/ntno.21942
59. Estelrich J, Busquets MA. Iron oxide nanoparticles in photothermal therapy. *Molecules*. 2018;23(7):1567. doi:10.3390/molecules23071567

60. Amzulescu MS, De Craene M, Langet H, et al. Myocardial strain imaging: review of general principles, validation, and sources of discrepancies. *Eur Heart J Cardiovasc Imaging*. 2019;20(6):605–619. doi:10.1093/ehjci/jez041
61. Purschke M, Laubach H, Anderson R, Manstein D. Thermal injury causes DNA damage and lethality in unheated surrounding cells: active thermal bystander effect. *J Invest Dermatol*. 2010;130(1):86–92. doi:10.1038/jid.2009.205
62. Xie W, Gao Q, Wang D, et al. Doxorubicin-loaded Fe3O4@MoS2-PEG-2DG nanocubes as a theranostic platform for magnetic resonance imaging-guided chemo-photothermal therapy of breast cancer. *Nano Res*. 2018;11(5):2470–2487. doi:10.1007/s12274-017-1871-1
63. Caltagirone C, Bettoschi A, Garau A, Montis R. Silica-based nanoparticles: a versatile tool for the development of efficient imaging agents. *Chem Soc Rev*. 2015;44(14):4645–4671. doi:10.1039/c4cs00270a
64. Cherian AM, Nair SV, Lakshmanan VK. The role of nanotechnology in prostate cancer theranostic applications. *J Nanosci Nanotechnol*. 2014;14(1):841–852. doi:10.1166/jnn.2014.9052
65. Yang K, Wan J, Zhang S, Zhang Y, Lee ST, Liu Z. In vivo pharmacokinetics, long-term biodistribution, and toxicology of PEGylated graphene in mice. *ACS Nano*. 2011;5(1):516–522. doi:10.1021/nn1024303
66. Zha L, Wang B, Qian J, et al. Preparation, characterization and preliminary pharmacokinetic study of pH-sensitive Hydroxyapatite/Zein nano-drug delivery system for doxorubicin hydrochloride. *J Pharm Pharmacol*. 2020;72(4):496–506. doi:10.1111/jphp.13223
67. Lee S, George Thomas R, Ju Moon M, et al. Near-infrared heptamethine cyanine based iron oxide nanoparticles for tumor targeted multimodal imaging and photothermal therapy. *Sci Rep*. 2017;7(1):2108. doi:10.1038/s41598-017-01108-5
68. Wang L, Xu X, Mu X, et al. Fe-doped copper sulfide nanoparticles for in vivo magnetic resonance imaging and simultaneous photothermal therapy. *Nanotechnology*. 2019;30(41):415101. doi:10.1088/1361-6528/ab2c13
69. Chen Y, Zhang F, Wang Q, et al. The synthesis of LA-Fe3O4@PDA-PEG-DOX for photothermal therapy-chemotherapy. *Dalton Trans*. 2018;47(7):2435–2443. doi:10.1039/c7dt04080f